Earth Planet. Sci. Lett. 679 (2026) 119879

Contents lists available at ScienceDirect

Earth and Planetary Science Letters

journal homepage: www.elsevier.com/locate/epsl

Structural heterogeneity and anisotropy beneath Myanmar: Insights into the complex deformation of the Indo-Burma subduction zone

Yiming Bai [a,b], Shengji Wei [c,d], Jing Chen [a], Tianjue Li [a], Bingfeng Zhang [a], Xiao Xiao [a], Shucheng Wu [e], Jiayuan Yao [f], Yu Wang [g], Ping Tong [a,b,c,*]

[a] School of Physical and Mathematical Sciences, Nanyang Technological University, Singapore 637371, Singapore
[b] Energy Research Institute, Nanyang Technological University, Singapore 637141, Singapore
[c] Earth Observatory of Singapore, Nanyang Technological University, Singapore 639798, Singapore
[d] Asian School of the Environment, Nanyang Technological University, Singapore 639798, Singapore
[e] State Key Laboratory of Geological Processes and Mineral Resources, China University of Geosciences, Wuhan 430074, China
[f] School of Geophysics and Geomatics, China University of Geosciences, Wuhan 430074, China
[g] Department of Geosciences, National Taiwan University, Taipei 106319, Taiwan

ARTICLE INFO

Edited by: Dr C Carolina Lithgow-Bertelloni

Keywords:
Oblique convergent margin
2025 Mw 7.8 Mandalay earthquake
Sagaing fault
Asthenospheric melt intrusion
Anisotropic tomography
Receiver function

ABSTRACT

The highly oblique Indo-Burma convergence has produced complex tectonic deformation along the Myanmar margin, and the depth-resolved anisotropy offers a valuable means to elucidate the mechanisms that drive this deformation. Here, we build a 3-D anisotropic body-wave velocity model in the upper 80 km using the adjoint-state traveltime tomography applied to an AI-assisted local earthquake catalog. The new model reveals pronounced azimuthal anisotropy and velocity heterogeneities. In the overriding Burma plate crust, a complex anisotropic structure is observed: fast velocity directions (FVDs) normal to the trench beneath the inner Indo-Burma Ranges while broadly parallel to the tectonic block boundaries and fault strikes beneath the Central Myanmar Basin. These patterns reflect transpressive deformation under oblique convergence. In the uppermost mantle, the observed ENE-WSW FVDs west of the Wuntho-Popa Arc are attributed to the fossil fabric in the subducting Indian plate, and the NNW-SSE FVDs farther east are associated with supra-slab along-strike flow, possibly shaped by the slab geometry complexity. Additionally, the segment of the Sagaing Fault near 21°N is likely infiltrated by crustal fluids originating from the adjacent Mogok Metamorphic Belt, potentially linked to recent asthenospheric melt upwelling. Evidence for fluid presence includes a near-fault crustal anomaly with ~8% velocity reduction, high *Vp/Vs* of >1.85 and FVDs parallel to the maximum horizontal compressive stress. Fluid infiltration likely promotes partial creep in this fault segment, and, together with variations in lithology and deformation state, may affect earthquake nucleation along this portion of the Sagaing Fault, including the 2025 Mw 7.8 Mandalay event.

1. Introduction

Myanmar in SE Asia lies above a complex plate configuration, where the Burma microplate is wedged between the Indian and Sunda plates and has accommodated their highly oblique, dextral wrench motion since the Eocene (Fig. 1a; Westerweel et al., 2019). The oblique Indo-Burma convergence has resulted in prominent deformation partitioning marked by fold-and-thrust shortening and purely strike-slip faulting (Steckler et al., 2016). At the eastern end of the Burma microplate, the Sagaing fault (SF) absorbs nearly half of the present-day dextral plate motion, with an average slip rate of ~20 mm/yr (Steckler et al., 2016; Tin et al., 2022). This ~1400 km-long fault runs nearly N-S from the Eastern Himalayan Syntaxis to the Andaman Spreading Center, traversing close to multiple large population centers in Myanmar, such as Mandalay, Naypyidaw and Yangon. Its high slip rate, simple geometry and proximity to urban areas render the SF arguably the greatest seismic hazard in Myanmar. Over the past two centuries, the SF has triggered at least ten destructive shallow earthquakes with magnitudes over 6.5, including the 2012 Mw 6.8 Thabeikkyin event and more recently the 2025 Mw 7.8 Mandalay event (Fig. 1b; Wang et al., 2014; Wei et al., 2025). The latter is the largest earthquake ever recorded instrumentally in the region and resulted in

* Corresponding author.
E-mail address: tongping@ntu.edu.sg (P. Tong).

https://doi.org/10.1016/j.epsl.2026.119879
Received 29 August 2025; Received in revised form 22 December 2025; Accepted 22 January 2026
Available online 29 January 2026

catastrophic damage, with 5352 direct fatalities in Myanmar and 103 in Thailand (en.wikipedia.org/wiki/2025_Myanmar-earthquake). Combined geodetic and seismic observations suggest that the 2025 event ruptured bilaterally and accelerated to supershear speeds exceeding 5 km/s during its southern propagation, with a total rupture length of >460 km, among the longest recorded for a continental strike-slip earthquake (Goldberg et al., 2025; Lindsey et al., 2025; Wei et al., 2025). Despite its significance, the seismogenic structure and environment that govern this earthquake at depth remain poorly understood. It is also noteworthy that although the SF is host to many large earthquakes, its ~250 km section between Mandalay and Naypyidaw had long been identified as a prominent seismicity gap from at least 1897 until the 2025 event, indicative of fault segmentation and changing interseismic slip mode (Hurukawa and Maung, 2011; Wang et al., 2014). Previous observations and simulations suggest that variations in fault roughness (i.e., frictional property), geometry, lithology, loading rate and environmental conditions (e.g., pore pressure or temperature) are potential factors modulating fault slip behavior (Bürgmann, 2018 and references therein). However, which of these factors, or combined, dominate the slip complexity along the SF, valuable for mitigating its seismic hazard posed to the region, remains vague.

The present-day tectonic setting of Myanmar is shaped by the Indo-Burma plate motion into four major N-S aligned units (Fig. 1a). To the west, the Indo-Burma Ranges (IBR) are traditionally viewed as the accretionary prism associated with the Indian oceanic plate subduction, and later developed into an arcuate fold-and-thrust mountain belt (Maurin and Rangin, 2009). The IBR consist of a western outer belt and an inner belt, both composed of strongly deformed Upper Cretaceous-Neogene sediments, as well as an eastern high-grade metamorphic core probably of Triassic age. East of the IBR across the Kabaw Fault (KF), the Central Myanmar Basin (CMB) comprises several pull-apart sub-basins filled with a thick stack of Paleogene-Neogene sedimentary succession (Bertrand and Rangin, 2003; P. Zhang et al., 2021). Along the central axis of the CMB, the Wuntho-Popa Arc (WPA) is characterized by scarce Neogene-Quaternary volcanic outcrops, notably at Popa and Monywa. In contrast to these WPA volcanics with a clear subduction origin, the Quaternary volcanics exposed at Singu, located east of the WPA near the SF, are geochemically more heterogeneous (Lee et al., 2016; Maury et al., 2004). East of and predating the SF, the Mogok Metamorphic Belt (MMB) records multiple episodes of low- to high-metamorphic and igneous events spanning Precambrian to Neogene (Barley et al., 2003; Searle et al., 2017). This ~50 km-wide belt extends SW from the Tibetan Plateau, interacts with the central SF and continues SSE along the Shan Scarps, forming the proto-boundary between the Burma and Sunda plates. Farther east, the Shan Plateau (SP) consists primarily of a Cambrian-Early Cretaceous metasedimentary sequence (Metcalfe, 2011). Two strike-slip fault networks are developed across the SP: a dominant ~E-W sinistral network likely associated with

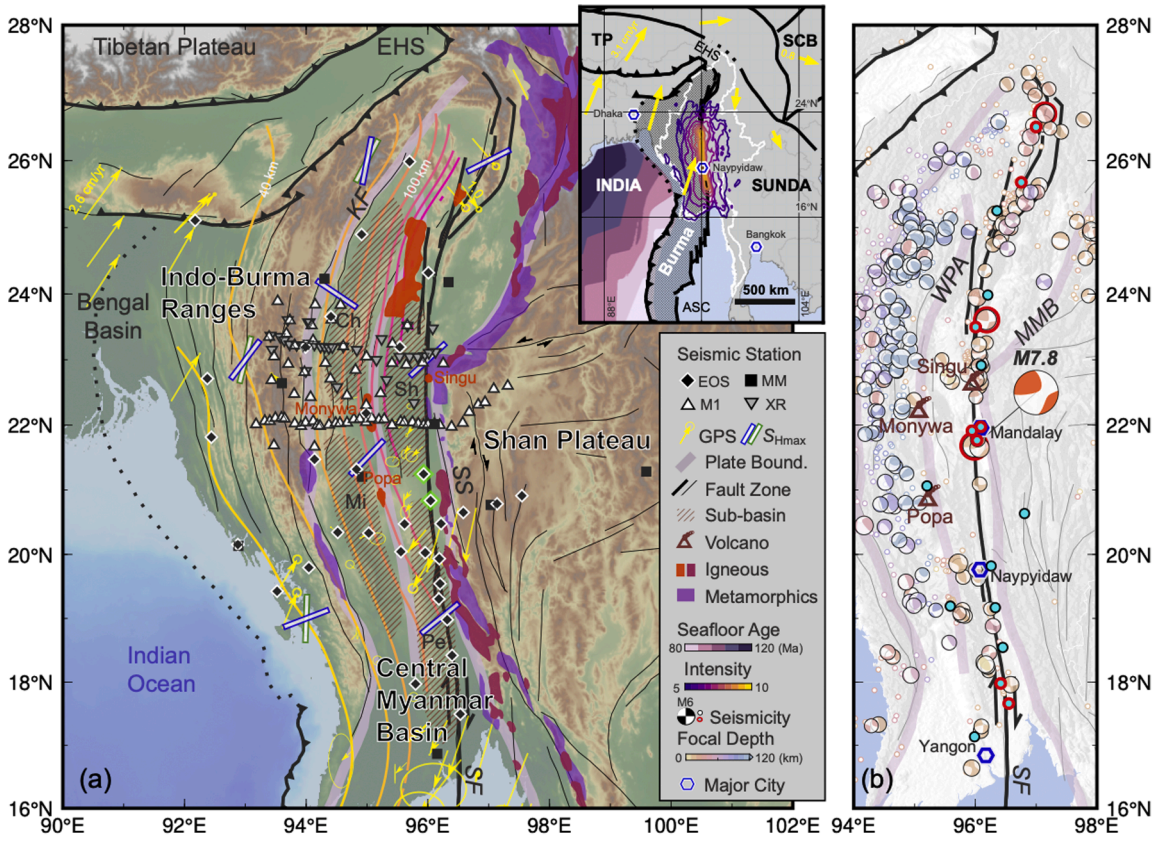

Fig. 1. Tectonic and geological background. (a) Regional map showing topography, GPS velocity vectors relative to the Burma plate, maximum compressive stress orientations in the crust (blue) and uppermost mantle (green) (Earnest et al., 2021), major tectonic boundaries and faults, Slab2 isodepths (Hayes et al., 2018), outcrops of metamorphic (purple), volcanic (orange) and intrusive (maroon) rocks, sub-basins and seismic stations (with the two along-SF stations used for *H-κ* stacking analysis ringed in green). The inset shows the simplified GPS velocities relative to the Asian plate, seafloor age and Modified Mercalli Intensity for the 2025 Mw 7.8 Mandalay earthquake (earthquake.usgs.gov/earthquakes/eventpage/us7000pn9s/map). (b) Earthquake distribution from the ISC-EHB catalog (color-coded by depth; isc.ac.uk/isc-ehb), paleoseismicity (cyan) and focal mechanisms for events with magnitudes over 5.0. The epicenter of the 2025 Mw 7.8 event is relocated at 96.10°E, 21.64°N (Wei et al., 2025). Earthquakes with Mw >6.5 are framed in red. Major cities and Quaternary volcanoes are superimposed. Abbreviations: TP - Tibetan Plateau; SCB - South China Block; EHS - Eastern Himalayan Syntaxis; ASC - Andaman Spreading Center; KF - Kabaw Fault; SF - Sagaing Fault; SS - Shan Scarps; Ch - Chindwin; Mi - Minbu; Sh - Shwebo; Pe - Pegu; WPA - Wuntho-Popa Arc; MMB - Mogok Metamorphic Belt. (For interpretation of the references to colour in this figure legend, the reader is referred to the web version of this article.)

the SE Tibetan Plateau extrusion, and a ~N-S dextral network narrowly distributed along the western SP margin near the SF, probably driven by plate convergence (Wang et al., 2014).

The tectonic responses to persistent Indo-Burma convergence have resulted in variations in the crustal and upper mantle structures, which have been detailed through multi-scale seismic imaging (e.g., Bai et al., 2020; Bai et al., 2021; Bertrand and Rangin, 2003; Li et al., 2008; Wang et al., 2019; Wu et al., 2021; Yao et al., 2021; G. Zhang et al., 2021; Zheng et al., 2020). Notably, the Moho offset across the SF-Shan Scarp system, in concert with on-fault seismicity down to >30 km depth (Fadil et al., 2023; Mon et al., 2020), indicates that this fault system penetrates the entire upper plate crust, estimated to be ~30–40 km thick (Wang et al., 2019; Zheng et al., 2020). Coupled mid-lower crustal high-velocity and uppermost mantle low-velocity anomalies imaged along the SF further point to mantle-derived magma intrusion along the fault and its subsequent cooling within the crust (Wu et al., 2021). Additionally, the eastward subduction of the Indian plate beneath Myanmar is evidenced by a low-velocity crustal layer with a dip angle of ~20° and a thickness of ~25–30 km in the upper 100 km, and a high-velocity lithosphere descending sub-vertically to the mantle transition zone (Bai et al., 2020; Yao et al., 2021; G. Zhang et al., 2021; Zheng et al., 2020). Estimates of seismic anisotropy can potentially yield information on past and current deformation. Existing anisotropic studies mainly concern the subduction dynamics and related mantle convection (e.g., Fan et al., 2024; Fan et al., 2021; Islam et al., 2024; Mohanty et al., 2024). Their results, based on shear-wave splitting of local and/or teleseismic *S* phases as well as azimuthal variation of Moho-converted *Ps* arrivals in receiver functions, provide depth-integrated estimates of anisotropy thus lack vertical resolution (Savage, 1999). On the other hand, available anisotropic tomographic models with depth sensitivity are at a continental level, thus unable to resolve fine-scale anisotropy changes, especially in the crust (e.g., Huang et al., 2015; Lü et al., 2017). A lithospheric anisotropic model across Myanmar is essential to fill in the resolution gap and to advance our knowledge on the deformation and dynamics of the Indo-Burma subduction zone.

Seismic anisotropy generally arises from three mechanisms: (1) Aligned, fluid-filled microcracks. Under differential stress, cracks perpendicular to the maximum compressive stress (S_{Hmax}) tend to close, while those aligned with the S_{Hmax} remain open (Boness and Zoback, 2006). This stress-induced anisotropy is typically confined to the brittle upper crust but can persist to greater depths when supported by high pore-fluid pressure (Savage, 1999). (2) Parallel fractures or fine layering of dissimilar lithologies. Anisotropy emerges when seismic wavelengths are much greater than the fracture or layer spacing, with fast waves polarized in the foliation plane defined by these macroscopic structures (Crampin et al., 1984). (3) Alignment of intrinsically anisotropic minerals. Lattice-preferred orientation (LPO) of anisotropic minerals formed during rock crystallization and modified by subsequent ductile deformation leads to bulk anisotropy. Most common rock-forming minerals in the crust, e.g., amphibole and mica, are anisotropic (Almqvist and Mainprice, 2017). Consequently, crustal rocks such as amphibolite, gneiss and schist can display strong anisotropy, although the overall anisotropy of these rocks is generally lower than that of individual crystals (Babuška and Cara, 1991). In the upper mantle, LPO of olivine is considered the dominant source of anisotropy (Zhang and Karato, 1995). Fast waves of anisotropy usually align with mantle flows (Savage, 1999; Zhao et al., 2016).

In this study, leveraging the broadband data recorded by multiple seismic experiments in and around Myanmar, we apply the adjoint-state traveltime tomography to a newly constructed, AI-assisted earthquake catalog to image the velocity heterogeneities and azimuthal anisotropy in the upper 80 km depths beneath the region. The resulting tomographic model is consistent with previous field and geophysical investigations while uncovering new features that potentially shed light on the widespread and intense lithospheric deformation beneath Myanmar and on the nation's natural hazard assessment.

2. Data and methods

We collect seismic data recorded by 140 broadband stations in Myanmar and its surrounding regions (92–98°E and 17–26°N) in the observation period from June 2016 to December 2022. Albeit less densely distributed (50–100 km spacing) south of 22°N than in the north (~10–50 km spacing), these stations provide fine coverage across the major geological units of the Indo-Burma subduction zone (Fig. 1a), which allows for an in-depth investigation of the subduction dynamics, regional deformation and seismotectonics.

2.1. Local earthquake traveltime data

To acquire the traveltime data for tomography, we build a new seismicity catalog for the Myanmar region via an AI-assisted workflow. Earthquake *P* and *S* phases are identified using the deep neural network-based model PhaseNet (Zhu and Beroza, 2019), pre-trained on the DiTing dataset from China (Zhao et al., 2022). The input data to PhaseNet are three-component seismic waveforms with a sampling rate of 100 Hz and bandpass filtered at 1–10 Hz. We retain picks with probabilities greater than 0.2 for both *P*- and *S*-wave phases. These picks are then associated with individual events using the spatiotemporal partitioning-accelerated PyOcto (Münchmeyer, 2024). For computational efficiency, we adopt a homogenous velocity model with fixed *Vp* of 7 km/s and *Vs* of 4 km/s, roughly equal to the mean values of recent 3-D regional models in the upper 80 km depths (Wu et al., 2021; G. Zhang et al., 2021). We require a minimum of 10 combined phases (at least 6 *P* and 4 *S* phases), a hypocentral distance ≤300 km, and an azimuthal gap <300° for successful earthquake location. We validate the AI-picked traveltimes by visually inspecting 1432 *P* and 1277 *S* phases from 100 randomly selected events, with a maximum of 20 events sampled per year from 2016 to 2022. Statistics shows that ~81 % of the traveltime differences between manual and AI picks are within 0.2 s (Fig. S1).

Absolute locations of individual earthquakes are improved using a probabilistic hypocenter inversion approach (Lomax et al., 2000). In this step, theoretical traveltimes are computed using a regional 1-D velocity model, where *Vs* is the horizontal average of the 3-D ambient noise tomographic model in Myanmar (Wu et al., 2021) and *Vp* is scaled empirically from *Vs* (Brocher, 2005). Following the relocation, we discard events with phase traveltime root mean square (RMS) >1.0 s and constrain the maximum traveltime residuals to 3.0 s for *P* phases and 6.0 s for *S* phases. In total, we obtain 144,673 *P* and 109,029 *S* traveltimes from 12,996 local earthquakes (Fig. 2a). The average RMS of these events is 0.81 s, and the average location uncertainties are ~3.61 km horizontally and ~4.92 km vertically. Furthermore, relative earthquake locations are refined using the double-difference method (Waldhauser and Ellsworth, 2000), with common-receiver differential traveltimes derived by direct catalog pick subtraction. 5826 events are relocated by this step, while the rest remain at their original single-event locations. We find the seismicity distribution in the new catalog broadly consistent with existing catalogs (Fadil et al., 2023; Mon et al., 2020; Mon et al., 2023; Yang et al., 2024), providing indirect evidence of its reliability.

We filter and weight the phase dataset prior to tomography to address the uneven data distribution and ensure comparable resolution of the *Vp* and *Vs* models. Specifically, we retain: (1) the event with the highest number of phase picks in each 0.08° × 0.08° × 0.5 km block; and (2) events recorded by at least six stations with both *P* and *S* phases. A box-weighting scheme (Text S1) is applied to further mitigate the influence of source and receiver clusters. Following these procedures, 46,751 first *P* and 46,751 first *S* traveltimes originating from 4651 earthquakes are selected (Fig. 2b). In the final traveltime dataset, ~40 % of the events are constrained by ≥10 stations with both *P* and *S* phases, and each station records at least nine events (Fig. S2). The average

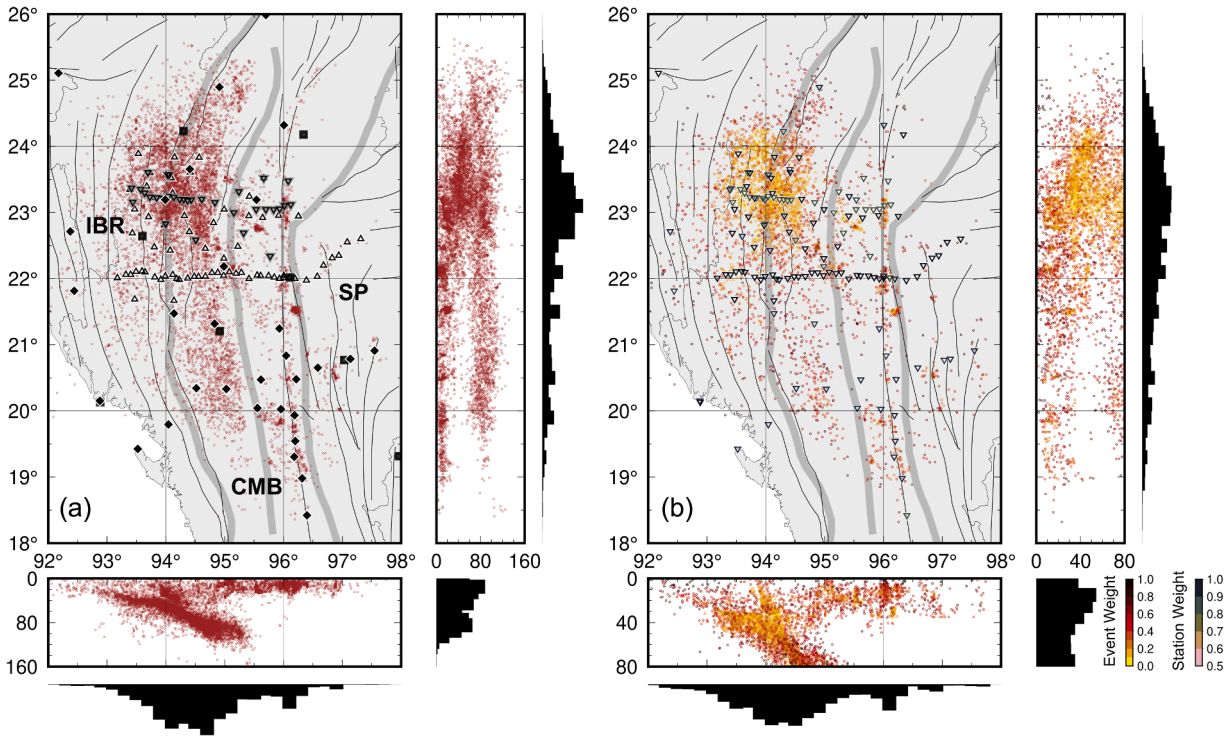

Fig. 2. Sesimic data coverage and selection. Distribution of (a) earthquakes in the newly constructed catalog and (b) the subset of earthquakes used for tomography. Each subfigure shows map views and corresponding cross-sectional projections along latitude and longitude, with histograms showing event counts. In (b), different colors denote the event and station weighting parameters applied in the tomographic inversion. IBR - Indo-Burma Ranges; CMB - Central Myanmar Basin; SP - Shan Plateau.

azimuthal gap is ~145°, with a maximum of 300°. We also test stricter station-count and azimuthal-gap thresholds, which alter the tomographic results to a limited degree.

2.2. Adjoint-state traveltime tomography

Using the data prepared in Section 2.1, we apply the adjoint-state traveltime tomography method (e.g., Tong, 2021) to invert for isotropic *Vp* and *Vs* structures and *Vp* azimuthal anisotropy from the surface to 80 km depth. This method is advantageous for its high accuracy in traveltime prediction through complex, anisotropic subsurface media, which is essential for constructing a reliable tomographic model. The objective of tomography is to derive an optimal model that minimizes the discrepancy between observed traveltimes $\mathbf{T}^{OBS}$ and model predictions $\mathbf{T}$ ($\mathbf{m}$):

$$\chi(\mathbf{m}) = \| \mathbf{T}(\mathbf{m}) - \mathbf{T}^{OBS} \|_2^2 \quad (1)$$

Sensitivity kernels of the misfit function with regard to slowness and anisotropic parameters are computed by solving the eikonal equation and the corresponding adjoint equation, using the fast-sweeping method (Luo and Qian, 2012). For accurate forward modelling, we design a dense propagation grid with a lateral and vertical spacing of 0.04° and 0.5 km, respectively. The inversion grid, determined through checkerboard resolution tests (Section 4.1), is evenly spaced laterally at 0.5° for slowness but coarser at 0.7° for the anisotropic parameters, which reflects a higher azimuthal data coverage required for anisotropy inversion. Vertically, we place 12 layers with increasing thickness with depth. A step-size-controlled gradient descent method is used to iteratively update the model parameters (Tong, 2021). A multiple-grid model parameterization, with 6 sets of staggered regular inversion grids, is adopted to discretize model perturbations (Tong et al., 2019).

We construct 3-D starting models for the inversion. For *Vs*, we employ the regional ambient noise tomographic model (Wu et al., 2021), with the initial *Vp* model scaled from *Vs* using Brocher (2005)'s empirical relation. *Vp* and *Vs* are inverted separately, each over 60 iterations. In every iteration of the *Vp* inversion, slowness and anisotropic parameters are updated first; the perturbed 3-D velocity model is then used to refine earthquake locations. The *Vs* inversion follows a similar procedure, except that anisotropy is ignored due to additional ambiguities, e.g., from *S*-wave birefringence. We also modify the objective function (Eq. (1)) in the *Vs* inversion by introducing a small perturbation to the observed *S* traveltimes:

$$\chi(\mathbf{m}) = \| \mathbf{T}_S(\mathbf{m}) - \left(\mathbf{T}_S^{OBS} + \mathbf{T}_P(\mathbf{m}_P) - \mathbf{T}_P^{OBS}\right) \|_2^2 \quad (2)$$

where $\mathbf{T}_P$ ($\mathbf{m}_P$) represents the *P* traveltimes predicted using the isotropic component of the final inverted *Vp* model. This modification is analogous to acquiring *Vp/Vs* by minimizing the misfit between synthetic and observed $\mathbf{T}_P$-$\mathbf{T}_S$. Eventually, both *Vp* and *Vs* inversions achieve >55 % reduction in data misfit. The RMS of *P*-wave traveltime residuals is reduced from 0.96 s to 0.40 s, and that of *S*-wave residuals from 1.76 s to 0.75 s (Fig. S3).

3. Results

3.1. Isotropic velocity

The new tomographic images reveal distinct velocity heterogeneities beneath Myanmar (Figs. 3–5). An overall good correlation is found between the *Vp* and *Vs* models. At crustal depths, seismic velocities are generally lower in the forearc region west of the WPA compared to the eastern back-arc region. More specifically, the velocity structure in the IBR crust is highly complicated. For instance, a narrow high-velocity anomaly (denoted by HV1) is imaged in the shallow crust beneath the IBR core, transitioning to relatively low velocities in the lower crust (e.g., Fig. 3d-3e). This feature is well-captured in the north but absent south of ~21.5°N, likely due to its narrow scale and sparser station coverage in

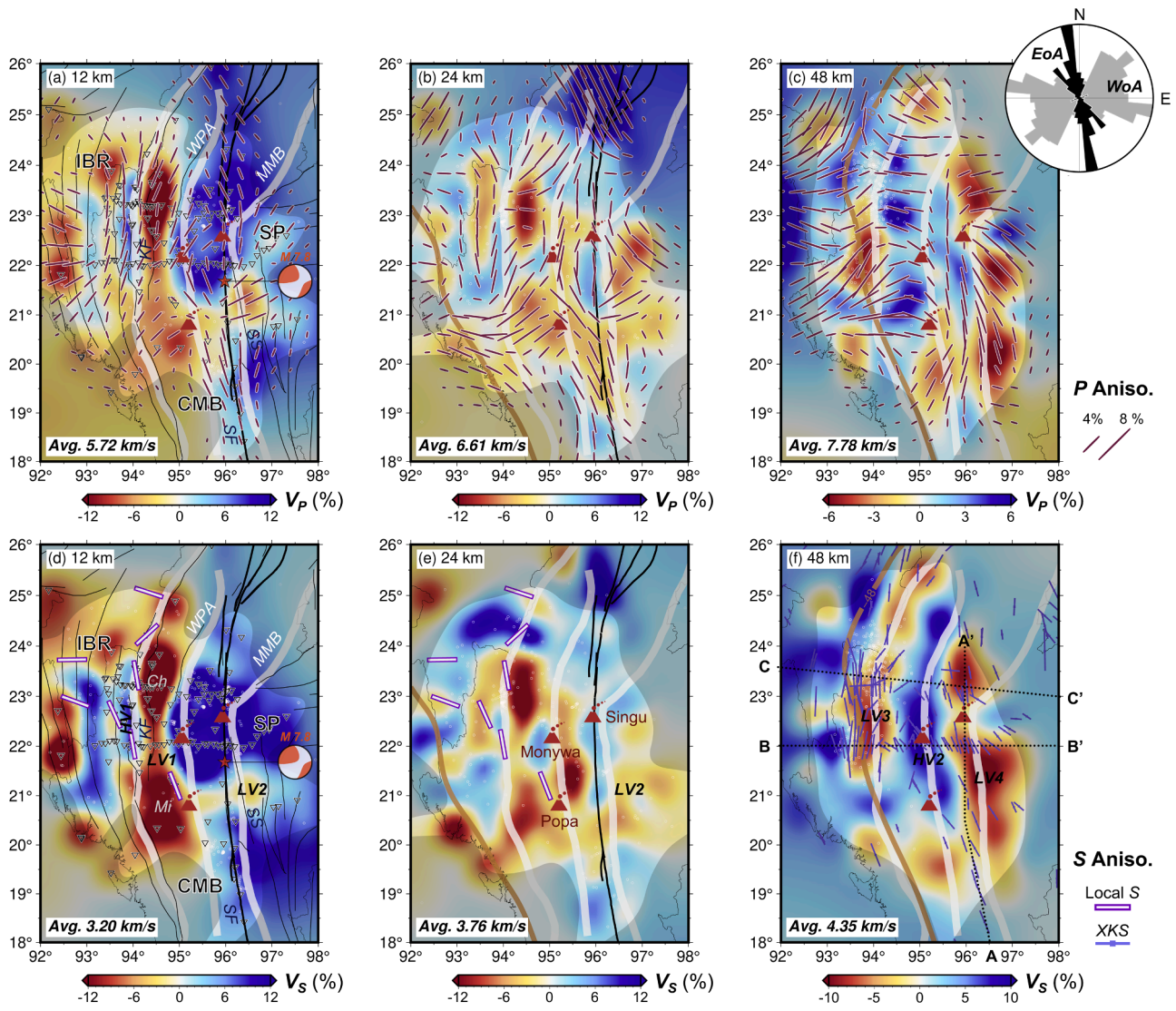

Fig. 3. Horizontal cross-sections of the tomographic model at representative depths. In each subfigure, the background map shows the velocity perturbation relative to the average value indicated in the bottom corner. HV1–2 and LV1–4 denote the key features identified in the model. Areas that are less well resolved are masked. The three thick white lines denote major tectonic boundaries. Brown lines mark the Slab2 isodepths (Hayes et al., 2018). Major faults (navy) and Quaternary volcanoes (red) are superimposed. In (a) and (d), the location of the Mw 7.8 event (Wei et al., 2025) is indicated by a star, with the corresponding focal mechanism as a beach ball. In (a-c), purple bars denote *Vp* azimuthal anisotropy. The rose map in (c) displays the statistics of FVDs east (EoA) and west (WoA) of the WPA. In (d-f), anisotropic measurements from previous *S*-wave splitting studies using local or telesesmic (*XKS*) events are shown (Fan et al., 2021; Islam et al., 2024; Mohanty et al., 2024). IBR - Indo-Burma Ranges; CMB - Central Myanmar Basin; SP - Shan Plateau; KF - Kabaw Fault; WPA - Wuntho-Popa Arc; SF - Sagaing Fault; SS - Shan Scarps.

the southern IBR. To be prudent, we only interpret features that can be reliably resolved by the data (e.g., Figs. S4-S5). East of the IBR, LV1 is a prominent low-velocity anomaly imaged beneath the forearc CMB, where both *Vp* and *Vs* decrease by >12 % in the upper crust (Fig. 3a and 3d). This LV1 extends to an apparent maximum depth of >20 km near 20.5°N and 23°N, corresponding to the depocenters of the Minbu and Chindwin sub-basins, respectively. By contrast, low-velocity anomalies beneath the back-arc CMB are weaker and confined to depths shallower than 10 km (Figs. 4–5). Farther east against the SF, LV2 with ~8 % velocity reduction is observed along the MMB at a restricted latitude range of ~21–22°N in the shallow crust, with the hypocenter of the 2025 Mw 7.8 earthquake located at its fringe (Fig. 3a and 3d; Wei et al., 2025). This anomaly becomes more dispersive with increasing depth. In the uppermost mantle, LV3 beneath the forearc, which is more pronounced in the *Vs* model (Fig. 3f), roughly aligns with the arc-shaped IBR. This anomaly appears disrupted at ~21°N. Eastward, beyond the relatively high-velocity uppermost mantle (HV2) beneath the WPA, strong low velocities (LV4) reappear beneath the SF and the SP (Fig. 3c and 3f). Fig. S6 presents complementary *Vp/Vs* images, and Fig. S7 shows an across-strike profile in the north.

3.2. Azimuthal anisotropy

Our model resolves a complex *P*-wave azimuthally anisotropic pattern across Myanmar (Fig. 3a-3c), which is a novel feature compared to previous tomographic studies in this region. In the shallow crust (e.g., at 12 km depth), FVDs below the inner IBR (west of ~94°E) trend perpendicular to its westerly convex strike, from NW-SE southward to NE-SW. Eastward beneath the IBR core and the CMB, however, FVDs rotate towards nearly N-S, broadly in line with the local features, except in the southern forearc, which is characterized by ~NE-SW aligned FVDs. At the CMB margins along the KF and the SF, anisotropy exhibits strong magnitude and predominantly a ~N-S FVD orientation. A noticeable exception occurs along the SF near 21°N, where FVDs deviate to a NE-SW direction oblique to the fault, corresponding almost perfectly to the presence of LV2 in the velocity model. Our restoration tests

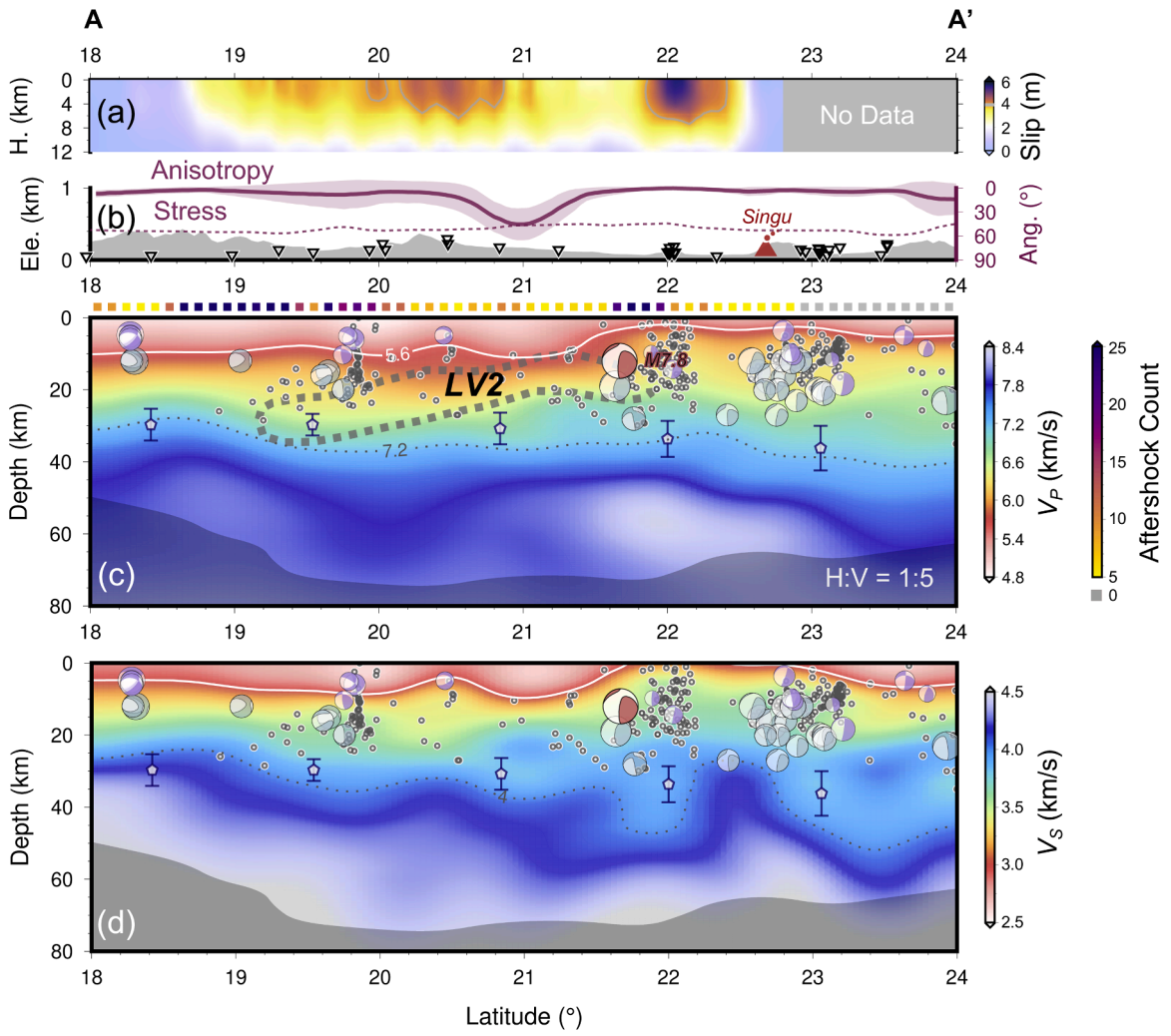

Fig. 4. Along-SF vertical cross-section (AA') of the tomographic model. The surface location is indicated in Fig. 3f. (a) Co-seismic slip of the 2025 Mw 7.8 event (Wei et al., 2025). Contours indicate the 4 m-slip. (b) Elevation, nearby seismic stations and the Singu volcano. The solid purple line shows the crust-averaged FVDs of anisotropy relative to the SF strike, with the shading area representing its standard deviation. As a comparison, the dashed line shows the orientation of S_{Hmax} along the SF trace. Below (b) also displays the aftershock counts of the Mw 7.8 events spanning 28/03/2025 to 15/04/2025, based on a regional catalog from the Thai Meteorological Department (TMD), Thailand. Note the reduced co-seismic slip and seismicity near 21°N, consistent with the presence of LV2 and the along-fault FVD deviation. (c-d) The (c) *Vp* and (d) *Vs* maps, respectively, with adjacent seismicity and focal mechanisms (blue - GCMT catalog; purple - Fadil et al., 2023) superimposed. The white and gray lines approximate the sedimentary base and the Moho interface, respectively, while the white dots with error bars represent Moho depths estimated by a previous joint inversion study (Wang et al., 2019). LV2 denotes the crustal low-velocity zone beneath the MMB, extracted from the *Vp* perturbation map. Note that the vertical scale is 5 times exaggerated.

support the reliability of this feature (Section 4.1). Farther east beneath the SP, anisotropy is comparatively weak, with FVDs trending N-S to NE-SW. In the lower crust (e.g., 24 km depth), the anisotropic structure becomes more complicated, possibly suggestive of a transitional regime between the crust and the uppermost mantle. It is noteworthy that the general fault-parallel FVDs along the SF and the distinct FVD deviation at ~21°N persist in most of the crust (Fig. 4b). In the uppermost mantle (e.g., 48 km depth), a clear dichotomy in FVD stands out, despite some localized variations. West of the WPA, FVDs are primarily trending E-W to NE-SW, while east of the WPA, they display a predominant NNW-SSE orientation.

4. Discussion

4.1. Resolution tests and comparison with previous models

Checkerboard and restoration tests are carried out to evaluate the resolving ability of our data and the robustness of the tomographic model (Text S2). The checkerboard test results suggest satisfactory recovery of anomalies with ≤10 % amplitude and lateral sizes of 0.75° for velocity and 1.0° for anisotropy, especially in densely instrumented areas, i.e., north of ~22°N and along the SF, where the main features in our model are detected (Fig. S4). In areas with sparser data coverage, e.g., the shallow crust beneath the southwestern area or the uppermost mantle beneath the northernmost area, smearing of velocity anomalies emerges, suggestive of reduced resolution. Velocity polarities and FVDs are evidently more reliable than amplitudes, which may be underestimated by up to ~3 %, especially at shallow depths where most rays sample the structure sub-vertically. The addition of random noise to the input data also partly contributes to the underestimation. Acknowledging this limitation, our interpretations are primarily based on qualitative patterns rather than exact amplitudes. We further design a restoration test to confirm the key features of interest (Fig. S5). It is clear that the velocity and anisotropy anomalies along the SF, the low-velocity structure beneath the CMB and its E-W extent, the low-velocity belt coinciding with the subducting Indian crust and its potential distortion

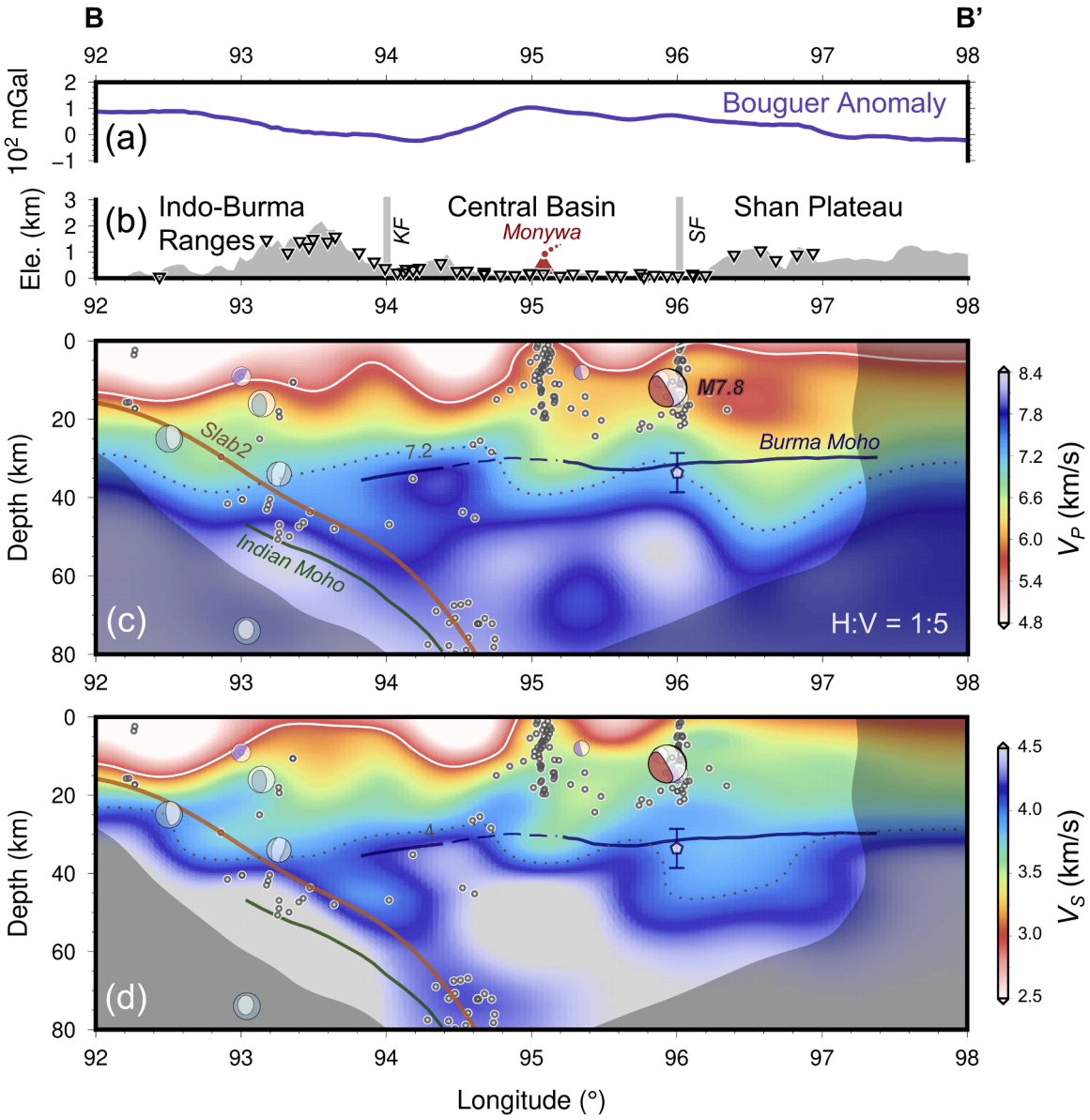

Fig. 5. Across-SF vertical cross-section (BB') of the tomographic model. The surface location is indicated in Fig. 3f. (a) Bouguer gravity along the SF. (b) Elevation, nearby seismic stations and the Monywa volcano. KF - Kabaw Fault; SF - Sagaing Fault. (c-d) The (c) *Vp* and (d) *Vs* maps, respectively, with adjacent seismicity and focal mechanisms (blue - GCMT catalog; purple - Fadil et al., 2023) superimposed. The white and gray lines approximate the sedimentary base and the Moho interface, respectively, while the white dots with error bars represent the Moho depths estimated by a previous joint inversion study (Wang et al., 2019). The Moho discontinuities of the upper and subducting plates from Bai et al. (2021) and the Slab2 model are superimposed. Note that the vertical scale is 5 times exaggerated.

at ~21°N, the high-velocity mantle wedge beneath the WPA, as well as the ~90°FVD rotation in the uppermost mantle are considerably robust, while some features, e.g., the longitudinal extent of HV1 beneath the IBR core, may be less reliable and should be interpreted with care. To investigate the potential trade-off between velocity heterogeneity and azimuthal anisotropy, we supplement an anisotropic *Vp* tomography using the isotropic component of the restoration model as the target. The results indicate minor leakage of <1 % between the velocity and anisotropic parameters in areas with dense data coverage (Fig. S5g-S5i). Nevertheless, a slightly increased coupling between parameters at greater depths (>35 km) becomes noticeable. Therefore, we focus on perturbations with amplitudes exceeding 1 % in the subsequent discussion. Using the real data, we further perform an isotropic *Vp* inversion and compare the misfit reduction with that from the anisotropic inversion. After five iterations, the anisotropic inversion yields ~21 % misfit reduction, faster than the ~17 % in the isotropic case. Incorporating anisotropy eventually contributes to an extra ~2 % misfit reduction over 60 iterations. These results demonstrate that anisotropic *Vp* parameterization allows improved data fitting.

Model reliability is supported by the general consistency between the isotropic component of our model and previous tomographic studies in spatially overlapped areas (e.g., Bai et al., 2021; Wu et al., 2021; G. Zhang et al., 2021), albeit small discrepancies probably arising from different data and methods used. At crustal depths (<~30 km), the sedimentary sequence in the forearc CMB is imaged as LV1. The prominent low-velocity, high *Vp/Vs* zone is clearly bounded by the KF to the west and the WPA to the east, in agreement with a localized Bouguer gravity high (Figs. 3, 5, S6-S7). This anomaly becomes less pronounced near 22°N, likely due to the combined effects of a topographic rise separating the northern Chindwin sub-basin from the southern Minbu sub-basin (P. Zhang et al., 2021) and high-velocity shallow-crustal solidified intrusions associated with the Monywa volcano (Figs. 3, 5c-5d;

G. Zhang et al., 2021). Assuming a *Vp* of 5.6 km/s and a *Vp/Vs* of 1.8 at the sediment base (G. Zhang et al., 2021), we estimate a maximum sedimentary thickness of ~20 km beneath the forearc CMB, comparable to the 18 km inferred from independent active-source surveys (e.g., Bertrand and Rangin, 2003; P. Zhang et al., 2021). By contrast, sediments in the back-arc CMB are much thinner. West of the CMB, the overall low velocities interspersed with strike-parallel high-velocity strips in the IBR crust align with the complex tectonics of the IBR, which formed as an accretionary prism consisting primarily of buoyant low-velocity sediments scrapped off at the trench from the downgoing Indian plate, and subsequently evolved into a fold-and-thrust belt, during which deeper and denser crustal materials may be brought to shallow levels. At depths greater than ~30 km, an east-dipping, low-velocity body LV3 is mapped that roughly follows the distribution of Benioff zone seismicity (Figs. 3, 5 and S7). This feature has been previously resolved and attributed by several previous studies to the crust of the subducting Indian plate (e.g., Bai et al., 2021; G. Zhang et al., 2021; Zheng et al., 2020). Our LV3 concurs with this interpretation and further indicates a potential distortion in the Indian crust at ~20–21°N, as implied by the absence of low velocities there (Fig. 3f). Moreover, the sub-arc mantle wedge is featured by the relatively high-velocity HV2, coinciding with the overall low Quaternary volcanic rate along the WPA (Maury et al., 2004). Nevertheless, localized low-velocity bodies are detected beneath the arc, hinting at the potential existence of arc magma-related aqueous fluid or partial melt: one sub-arc low-velocity anomaly is positioned in the uppermost mantle below Monywa (Fig. 5c), and is also discernible in previous tomographic images (Bai et al., 2021; G. Zhang et al., 2021); another is in the lower crust beneath Mt. Popa and its north without reaching Monywa, and has not yet been reported (Fig. 3e). However, due to limited station coverage in the Popa area, the definitive origin of this anomaly will be addressed in future studies. Along the SF, previous ambient noise tomography identifies a striking low-velocity feature beneath the Moho, interpreted as magma ponding under the crust (Wu et al., 2021). This feature corresponds to our LV4, which is slightly offset to the east and more closely aligned with the MMB (Fig. 3c and 3f). In addition to structural heterogeneities compatible with existing observations, our model reveals several new features, particularly in terms of azimuthal anisotropy, which will be detailed in the following sections.

4.2. Diverse deformation in the Indo-Burma subduction zone

4.2.1. Crust

From west to east, FVDs in the Bruma crust are roughly trench-normal in the inner IBR, but transition broadly to trench parallel into the IBR core and the CMB. This pattern is generally consistent with the crustal depth-integrated measurements in the area (Fig. 3d-3e; Fan et al., 2024; Fan et al., 2021; Mohanty et al., 2024), and corroborates the oblique subduction-controlled deformation partitioning (Steckler et al., 2016). Since the nearly trench-perpendicular FVDs beneath the inner IBR are at a high angle to major ~N-S striking faults and the present-day stress field, with the S_{Hmax} subparallel to the northeastward Indian plate motion (Fig. 1a; Earnest et al., 2021; Mon et al., 2020), the anisotropy there is unlikely to be controlled by either local structure or stress-induced microcracks. A plausible alternative explanation is the LPO of deformed minerals, such as amphibole, which is found abundant in the continental lower crust and has been identified in Lower Miocene sandstones of the IBR (Khin et al., 2017). Laboratory experiments demonstrate that amphibole-bearing rocks under compressive pure shear can generate strong *Vp* anisotropy (up to 16 % at 600 MPa; Ji et al., 1993; Ji et al., 2015), which can fully account for the observed <8 % strike-normal anisotropy. Eastward in the highly metamorphosed schist-gneiss belt of the IBR core (Khin et al., 2017; Maurin and Rangin, 2009), the pronounced strike-slip shearing, e.g., along the KF, may orient the FVDs of azimuthal anisotropy within the foliation plane parallel to the ~N-S fault strikes (Almqvist and Mainprice, 2017; Ji et al., 2015).

Beneath the CMB, the nearly along-arc FVDs may be attributed to inclined sedimentary bedding, prominently in the shallow crust, and shear faulting across a broader depth range. The latter interpretation is supported by active-source surveys (e.g., P. Zhang et al., 2021) and more recent earthquake relocation studies, which identify multiple along-strike hidden faults in the CMB crust hosting dextral earthquakes (Mon et al., 2020; Yang et al., 2024). These faults, similar to the major SF, may absorb the strike-slip deformation of the oblique subduction (Mon et al., 2020). We note, however, that deviations from the dominant arc-parallel pattern are imaged at certain positions, e.g., west of the Popa volcano (Fig. 3a-3b). These anomalies could potentially result from limited azimuthal data coverage in the southern forearc, although resolution tests indicate fairly retrieved FVDs (Fig. S5). If reliable, these variations might reflect changing crustal deformation along the strike, which is echoed by the more intense forearc seismicity north of ~22°N than in the south (Fig. 2). Further validation relies on additional data.

4.2.2. Uppermost mantle

The observed anisotropy exhibits a more coherent FVD pattern in the uppermost mantle than in the crust (Fig. 3c). We observe trench-normal (ENE-WSW) oriented FVDs in the western study area, where motions of the downgoing Indian plate dominate. This orientation is in marked contrast with the NNW-SSE to N-S oriented FVDs inferred by teleseismic *S*-wave splitting beneath the area (Fig. 3f). The latter is thought to predominately reside beneath the subducting plate, where trench-parallel sub-slab mantle flow may be developed (Fan et al., 2021; Islam et al., 2024; Mohanty et al., 2024). Conversely, our observed anisotropy in the Indian plate may originate from either subduction-related active deformation or the fossil fabric formed during plate formation at a mid-ocean ridge (Eakin et al., 2015; Plomerová and Babuška, 2010). Previous studies indicate that plate bending can modify anisotropy through strain-induced LPO (Eakin et al., 2015). The trench-normal extension produced by bending in the upper part of the Indian plate, with a moderate dip angle of ~20°, may generate trench-normal FVDs, as it typically occurs under ductile deformation at depth (Zhao et al., 2016). This interpretation is echoed by nearly along-trench S_{Hmax} within the slab (Fig. 1a; Earnest et al., 2021). However, there is a debate over whether slab bending/unbending produces sufficient strain to form mineral LPO in the upper part of the slab (Kaminski and Ribe, 2002). Alternatively, the fossil fabric hypothesis predicts FVDs perpendicular to seafloor magnetic lineation, which trends NNE-SSW in the Indian Ocean, compatible with our observations (Figs. 1a and 3c). We therefore lean to the interpretation that the ENE-WSW anisotropy in the upper section of the slab represents a preserved fabric.

Along the subduction direction, the trench-normal FVDs terminate beneath the WPA, east of which they rotate to trench parallel (NNW-SSE). Similar ~90° variation in FVDs is well captured by *Pn* anisotropy in the mantle lid (Lü et al., 2017). Teleseismic *S*-wave splitting studies also reveal an along-trench fast *S*-wave polarization direction in the back-arc region, with the dominant source of anisotropy estimated at ~40–80 km depths (Fan et al., 2021; Islam et al., 2024). The agreement among different anisotropic observations for the same area underscores confidence in our tomographic model. A plausible explanation for the trench-parallel anisotropy in the back-arc uppermost mantle could be 3-D mantle flow induced by complex geometry and/or rollback of the subducting Indian plate (e.g., Fan et al., 2021; Lee et al., 2016). Similar trench-parallel anisotropy due to supra-slab mantle flow has been documented in other oblique subduction systems, such as Alaska, Kuril and Izu-Bonin (Zhao et al., 2016). The complex slab geometry that may promote this back-arc flow beneath Myanmar is supported by a distortion in the subducting Indian crust at ~21°N, as inferred from our velocity model (Fig. 3c and 3f). This latitude also coincides with a southward decrease in subduction obliquity, a gap in intermediate-depth seismicity, and a potential slab tear in the upper

mantle (e.g., Bai et al., 2020; Li et al., 2008). Farther east outside our study area, Islam et al. (2024) show that the trench-parallel anisotropy rotates again back to ~E-W, possibly reflecting a geodynamic regime unnecessarily related to the Indian plate subduction.

4.3. Fluid infiltration into the central SF

Our tomographic model newly resolves a crustal feature LV2 that is located almost entirely east of the SF beneath the MMB in the shallow crust and spreads out at greater depths (Figs. 3 and 4c). To better understand this feature, we quantitatively estimate *Vp/Vs*, a property more sensitive to compositional variations and the presence of fluids or partial melt compared to *Vp* or *Vs* alone (Christensen, 1996; Takei, 2002). Independent *H-κ* stacking analysis using receiver functions at the two stations nearest LV2 shows that the *Vp/Vs* averaged in the crust ranges in ~1.85–1.90 (Figs. 6 and S8; Text S3), much higher than the global continental average of ~1.77 (Christensen, 1996). Laboratory experiments indicate that *Vp/Vs* higher than 1.82 can be attributed to the increment of crustal melt, assuming that other effects such as temperature or melt geometry are minor (Takei, 2002; Watanabe, 1993). The concurrence of elevated *Vp/Vs* and reduced seismic velocities supports the presence of fluids (aqueous and/or partial melt) in the crust. Following Feng et al. (2023), the estimated *Vp/Vs* of 1.85–1.90 corresponds to a ~6–9 % fluid fraction (Fig. 6; Text S4). Meanwhile, we observe that this LV2 is accompanied by a clear change in anisotropy: NE-SW oriented FVDs within LV2, compared to the otherwise N-S to NNW-SSE FVDs along the SF trace (Fig. 4b). Remarkably, the anomalous NE-SW orientation aligns with the S_{Hmax} of the ambient stress field (Fig. 1a). This correlation indicates that stress-induced anisotropy, with FVDs parallel to the S_{Hmax}, likely dominates in LV2. The presence of fluids with high pore pressure would allow microcracks to remain open at a broader depth range, enhancing this anisotropic feature (Almqvist and Mainprice, 2017; Savage, 1999).

Below LV2, still along the MMB, occupies the pronounced LV4 of

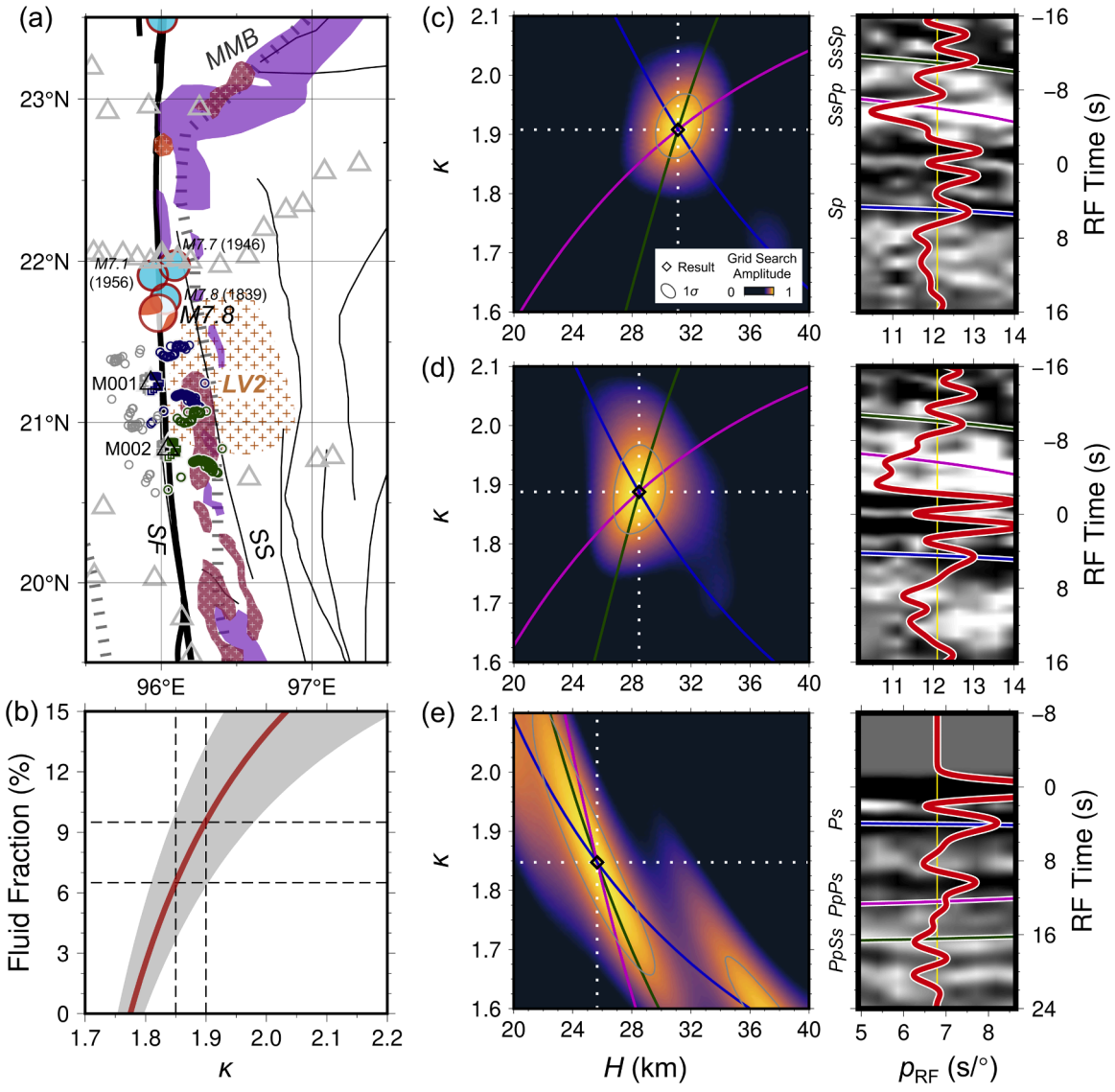

Fig. 6. *H-κ* stacking analysis and fluid fraction estimation. (a) Data coverage. Circles and squares denote *S*- and *P*-wave receiver function piercing points near the Moho (30 km depth), respectively. Only events nearer LV2, i.e., those from the east, are adopted in the analysis. LV2 denotes the crustal low-velocity anomaly beneath the MMB at 12 km depth, where the hypocenter of the 2025 Mw 7.8 event is located. See Fig. 1 for information on the other graphic elements. (b) Fluid fraction estimation. The red curve represents the predicted relationship between *Vp/Vs* and fluid fraction, with the corresponding uncertainties shaded in gray. Crosshair lines denote the estimated melt fraction range using a preferred set of parameters (Text S4). (c) *H-κ* stacking result using *S*-receiver functions at station M001 (left) and the corresponding waveforms (right). The Moho-derived receiver function phases are labeled. (d) Same as (c), but for *S*-receiver functions at M002. (e) Same as (c-d), but for *P*-receiver functions at M002 after sediment-effect removal, yielding sub-sediment crustal thickness and *Vp/Vs*.

relatively low velocities and high *Vp/Vs* in the uppermost mantle (Figs. 3c, 3f and S6). This LV4 can be traced downward into the asthenosphere (i.e., >80 km depths), where it merges with a broader low-velocity zone previously imaged beneath the SP and SE Tibet (e.g., Feng et al., 2020). The apparent continuity of low-velocity and high-*Vp/Vs* anomalies from the shallow crust to the asthenosphere along the MMB supports a recent asthenospheric melt intrusion process (Fig. 7), possibly in response to slab rollback and associated back-arc extension (Bertrand and Rangin, 2003; Lee et al., 2016). This interpretation is reinforced by geological evidence of alkaline mafic basalt occurrences at several sites within the MMB, notably at the Quaternary Singu volcano located north of LV2 on top of the SF-Shan Scarp system (Fig. 6; Maury et al., 2004; Searle et al., 2017). Geochemical analyses of the Singu volcanics reveal a clear asthenospheric signature, which contrasts to the subduction-related compositional characteristics of the WPA volcanics (Lee et al., 2016; Maury et al., 2004). Asthenospheric melt is typically focused along regional lithospheric weaknesses, in our case most likely the boundary between the Burma and Sunda plates, i.e., the SF-Shan Scarp system. Melt may stall in the uppermost mantle and lower crust, supplying the heat necessary for the latest Oligocene-Middle Miocene metamorphism and partial melting in the MMB (Barley et al., 2003; Searle et al., 2017), which in turn released crustal fluids. These melt and fluids may ascend further into the shallow crust, for instance via the network of secondary dextral faults beneath the southern SP (Fig. 1a; Wang et al., 2014), where they could remain trapped to the present day. This provides a plausible explanation for the origin of LV2, its high *Vp/Vs* and the S_{Hmax}-parallel FVDs. Along the SF portions away from LV2, and possibly with limited fluid involvement, the fault-parallel FVDs may reflect a joint influence of the shear-induced fault fabric and mineral foliation in the solidified igneous and metamorphic rocks.

Our interpretation offers new insights into the seismogenesis of the SF. Fluids infiltrating the SF segment near LV2 may act like lubricants, promoting partial creep instead of fast earthquake rupture (e.g., Di Toro et al., 2006). A similar case has been reported along the San Andreas Fault near Parkfield (e.g., Becken and Ritter, 2012). While geodetic data indicate a steady slip rate of ~23–24 mm/yr along the central SF (Tin et al., 2022), the fault section juxtaposed to the inferred fluid-rich LV2 is characterized by reduced seismicity and a comparably shallow seismogenic depth of ~10 km (Fadil et al., 2023). This section had also been recognized as a >100-year seismicity gap prior to the 2025 Mw 7.8 earthquake (Hurukawa and Maung, 2011). Further support for partial creep comes from the subdued aftershocks and relatively small co-seismic slip associated with the Mw 7.8 event in this fault segment (Fig. 4), characteristics typical of fluid-affected faults (Marguin and Simpson, 2023), albeit the reduced slip could also reflect re-rupture of an earlier break (Lindsey et al., 2025). South of this segment, the Mw 7.8 event rupture accelerated to supershear (Goldberg et al., 2025), though pending validation on the potential link between supershear rupture and fluid presence. Additionally, serpentinites that are found cropping out along the SF may also promote fault creep (Morishita et al., 2023).

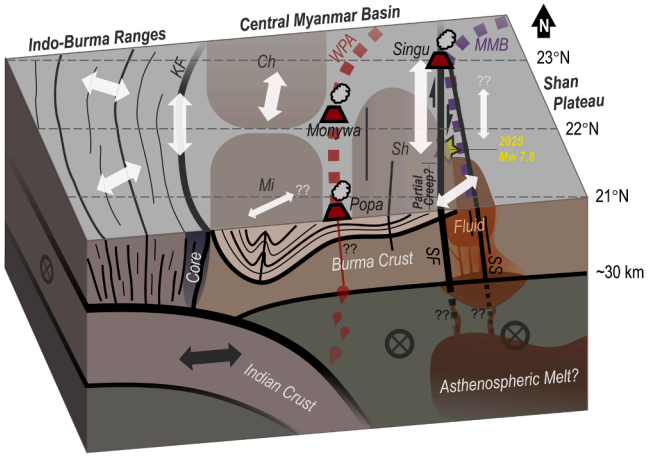

Fig. 7. Cartoon summarizing the primary findings of this work. White arrows on the surface show the predominant FVDs of crustal azimuthal anisotropy; those marked with question marks require further validation with additional data. Black arrows in the depth profiles show the predominant FVDs in the uppermost mantle. Major tectonic units are also shown. WPA - Wuntho-Popa Arc; MMB - Mogok Metamorphic Belt; KF - Kabaw Fault; SF - Sagaing Fault; SS - Shan Scarps; Ch - Chindwin basin; Mi - Minbu basin; Sh - Shwebo basin. See Sections 4.2–4.3 for more details.

On the other hand, the short SF segment and its nearby faults immediately north of LV2 have nucleated at least four Mw >7.0 earthquakes, including the 2025 event (Figs. 1b and 6a). Our tomographic model clearly reveals that these strong earthquakes occurred within the high-velocity section of a high-to-low velocity transition, which delineates LV2 inferred to host fluids in the south from a more rigid, high-velocity zone strengthened by exhumed metamorphic rocks to the north (Figs. 4 and 6a). Similar fluid-related velocity contrasts have been linked to large earthquake genesis globally (Zhao et al., 2002). Moreover, azimuthal anisotropy across this transition shows a prominent variation in FVD, a clear indicator of change in stress state (e.g., Fig. 4b). These findings collectively highlight that along-strike variations in rock properties, fluid content and deformation styles may effectively modulate the slip behavior and earthquake nucleation along the SF. Other structural factors, such as a fault polarity reversal identified at ~21.5°N (Tin et al., 2022), might also contribute to this complexity. Fault segments undegoing creeps are often delineated by small, repetitive low-frequency earthquakes (e.g., Becken and Ritter, 2012). However, these earthquakes may not be reliably detected by our AI picker, especially considering the relatively coarse data coverage (with a > 50 km average station interval) near the SF (Fig. 2). A denser array would be helpful to clarify this issue.

5. Conclusions

We apply the adjoint-state traveltime tomography to an AI-assisted local earthquake catalog to image the lithospheric-scale anisotropic velocity structure beneath the Myanmar region. The inverted velocity model agrees well with surface geology and prior geophysical observations, while additionally resolving strong lateral and vertical changes in azimuthal anisotropy (Fig. 7) that were largely overlooked in previous regional studies.

Our model reveals complicated crustal anisotropic features in the upper Burma plate, reflecting deformation partitioning driven by the active oblique convergence between the Indian and Burma plates. FVDs nearly perpendicular to the trench beneath the inner IBR can be attributed to mineral LPO formed under strong shortening, while those along major boundary faults (e.g., the KF and the SF) and along the arc beneath the CMB may largely result from shear-induced macroscopic alignment. In the uppermost mantle, a pronounced anisotropic contrast is resolved. Across-strike FVDs west of the WPA in the area entrained by the subducting Indian plate motion likely reflect the fossil fabric in the slab, while along-strike FVDs farther to the east may indicate supra-slab mantle flow, potentially initiated due to the complicated 3-D slab geometry, as inferred from a possible dent in the Indian crust.

A key feature in our model is a crustal low-velocity zone focused at ~21°N beneath the MMB. Combining this with high *Vp/Vs* of >1.85 estimated independently by receiver functions and anomalous S_{Hmax}-parallel FVDs beneath the area supports the presence of magmatic-metamorphic fluids. The intrusion of low-velocity anthenosphere-derived melt along the SF-Shan Scarp system may supply the necessary heat to the crustal fluid-generation processes. Fluid infiltrating the central segment of the SF likely modulates its slip behaviors by promoting partial creep, while the areas immediately to the north under restricted fluid effect appears more susceptible to large earthquakes, including the 2025 Mw 7.8 Mandalay event. These observations stress a

potential link between earthquake nucleation and variations in fluid content, rock property and deformation state along the SF, a topic that warrants further investigations.

Data resources

Seismic waveform data from the Myanmar National Seismic Network and Tripartite-BIMA are available at ds.iris.edu/mda/MM/ and ds.iris.edu/mda/XR_2018/, respectively. The earthquake waveforms and catalog of the China-Myanmar Geophysical Survey of the Myanmar Orogen (Phase I) can be accessed through Yang et al. (2024). The waveform data from the EOS-Myanmar and EOS-Bangladesh networks used in this study are available upon reasonable request from the corresponding author. The newly constructed local earthquake catalog and final velocity model are deposited at 10.6084/m9.figshare.30000577.

CRediT authorship contribution statement

Yiming Bai: Writing – original draft, Visualization, Investigation, Data curation, Conceptualization. **Shengji Wei:** Writing – review & editing, Resources, Data curation. **Jing Chen:** Writing – review & editing, Software, Methodology. **Tianjue Li:** Writing – review & editing, Resources. **Bingfeng Zhang:** Writing – review & editing, Resources. **Xiao Xiao:** Writing – review & editing, Resources. **Shucheng Wu:** Resources. **Jiayuan Yao:** Resources. **Yu Wang:** Resources. **Ping Tong:** Writing – review & editing, Supervision, Methodology, Funding acquisition, Conceptualization.

Declaration of competing interest

The authors declare that they have no known competing financial interests or personal relationships that could have appeared to influence the work reported in this paper.

Acknowledgements

This research is funded by the Indonesian Endowment Fund for Education (LPDP) on behalf of the Indonesian Ministry of Education, Culture, Research, and Technology and managed under the INSPIRASI Program (Grant Number: 2924/E3/AL.04/2024 and 4809/UN.I/PK.08.00/2024) and the Singapore Ministry of Education (MOE) Academic Research Fund (AcRF) Tier 2 Grant (MOE-T2EP20124-0003). We thank all the participants for their dedication to the seismological observations in and around Myanmar. We also thank the Earthscope SAGE Data Center for servicing the open-access data. We appreciate the helpful comments from Carolina Lithgow-Bertelloni (Editor), Tuncay Taymaz, and an anonymous referee. Y. Bai acknowledges Shun Yang and Enbo Fan for useful discussion on Myanmar seismology. Most of the figures are generated by PyGMT (10.5281/zenodo.15628725). We use SeisBench (seisbench.readthedocs.io/en/stable/) for earthquake phase picking and association; NonlinLoc (alomax.free.fr/nlloc/) and HypoDD (www.ldeo.columbia.edu/~felixw/hypoDD.html) for single- and multi-event relocations, respectively. TomoATT (tomoatt.com/) is applied for seismic tomography. Computational work was performed using resources of the National Supercomputing Centre, Singapore (www.nscc.sg).

Supplementary materials

Supplementary material associated with this article can be found, in the online version, at doi:10.1016/j.epsl.2026.119879.

Data availability

The links to data/code have been included in Data Resources.

References

Almqvist, B.S.G., Mainprice, D., 2017. Seismic properties and anisotropy of the continental crust: predictions based on mineral texture and rock microstructure. Rev. Geophys. 55, 367–433. https://doi.org/10.1002/2016RG000552.

Babuška, V., Cara, M., 1991. Seismic Anisotropy in the Earth. Springer Science & Business Media.

Bai, Y., He, Y., Yuan, X., Tilmann, F., Ai, Y., Jiang, M., Hou, G., Mon, C.T., Thant, M., Sein, K., 2021. Seismic structure across central Myanmar from joint inversion of receiver functions and Rayleigh wave dispersion. Tectonophysics 818, 229068. https://doi.org/10.1016/j.tecto.2021.229068.

Bai, Y., Yuan, X., He, Y., Hou, G., Thant, M., Sein, K., Ai, Y., 2020. Mantle transition zone structure beneath Myanmar and its geodynamic implications. Geochem. Geophys. Geosyst. 21, e2020GC009262. https://doi.org/10.1029/2020GC009262.

Barley, M.E., Pickard, A.L., Zaw, K., Rak, P., Doyle, M.G., 2003. Jurassic to miocene magmatism and metamorphism in the Mogok metamorphic belt and the India-Eurasia collision in Myanmar: magmatism and metamorphism in the mogok belt. Myanmar Tecton. 22. https://doi.org/10.1029/2002TC001398 n/a-n/a.

Becken, M., Ritter, O., 2012. Magnetotelluric studies at the San Andreas Fault Zone: implications for the role of fluids. Surv. Geophys. 33, 65–105. https://doi.org/10.1007/s10712-011-9144-0.

Bertrand, G., Rangin, C., 2003. Tectonics of the western margin of the Shan plateau (central Myanmar): implication for the India–Indochina oblique convergence since the Oligocene. J. Asian Earth. Sci. 21, 1139–1157. https://doi.org/10.1016/S1367-9120(02)00183-9.

Boness, N.L., Zoback, M.D., 2006. Mapping stress and structurally controlled crustal shear velocity anisotropy in California. Geology. 34, 825–828. https://doi.org/10.1130/G22309.1.

Brocher, T.M., 2005. Empirical relations between elastic wavespeeds and density in the earth's crust. Bull. Seismol. Soc. Am. 95, 2081–2092. https://doi.org/10.1785/0120050077.

Bürgmann, R., 2018. The geophysics, geology and mechanics of slow fault slip. Earth. Planet. Sci. Lett. 495, 112–134. https://doi.org/10.1016/j.epsl.2018.04.062.

Christensen, N.I., 1996. Poisson's ratio and crustal seismology. J. Geophys. Res. Solid. Earth. 101, 3139–3156. https://doi.org/10.1029/95JB03446.

Crampin, S., Chesnokov, E.M., Hipkin, R.G., 1984. Seismic anisotropy — the state of the art: II. Geophys. J. Int. 76, 1–16. https://doi.org/10.1111/j.1365-246X.1984.tb05017.x.

Di Toro, G., Hirose, T., Nielsen, S., Pennacchioni, G., Shimamoto, T., 2006. Natural and experimental evidence of melt lubrication of faults during earthquakes. Science 311, 647–649. https://doi.org/10.1126/science.1121012.

Eakin, C.M., Long, M.D., Wagner, L.S., Beck, S.L., Tavera, H., 2015. Upper mantle anisotropy beneath Peru from SKS splitting: constraints on flat slab dynamics and interaction with the Nazca Ridge. Earth. Planet. Sci. Lett. 412, 152–162. https://doi.org/10.1016/j.epsl.2014.12.015.

Earnest, A., Sunilkumar, T.C., Silpa, K., 2021. Sinking slab stress and seismo-tectonics of the Indo-Burmese arc: a reappraisal. Tectonics 40. https://doi.org/10.1029/2021TC006827.

Fadil, W., Wei, S., Bradley, K., Wang, Y., He, Y., Sandvol, E., Huang, B., Hubbard, J., Thant, M., Htwe, Y.M.M., 2023. Active faults revealed and new constraints on their seismogenic depth from a high-resolution regional focal mechanism catalog in Myanmar (2016–2021). Bull. Seismol. Soc. Am. https://doi.org/10.1785/0120220195.

Fan, E., Ai, Y., Gao, S.S., He, Y., Liu, K.H., Jiang, M., Hou, G., Yang, S., Mon, C.T., Thant, M., Sein, K., 2024. Mantle flow and olivine fabric transition in the Myanmar continental subduction zone. Geology. https://doi.org/10.1130/G51698.1.

Fan, E., He, Y., Ai, Y., Gao, S.S., Liu, K.H., Jiang, M., Hou, G., Mon, C.T., Thant, M., Sein, K., 2021. Seismic anisotropy and mantle flow constrained by shear wave splitting in Central Myanmar. J. Geophys. Res. Solid. Earth. 126, e2021JB022144. https://doi.org/10.1029/2021JB022144.

Feng, M., An, M., Mechie, J., Zhao, W., Xue, G., Su, H., 2020. Lithospheric structures of and tectonic implications for the central–east Tibetan plateau inferred from joint tomography of receiver functions and surface waves. Geophys. J. Int. 223, 1688–1707. https://doi.org/10.1093/gji/ggaa403.

Feng, M., Wei, S., Chen, L., Muksin, U., Lythgoe, K., Wang, T., Wu, Z., 2023. Pervasive crustal volcanic mush in the highly stretched Sunda Plate margin of Northern Sumatra. Geophys. Res. Lett. 50, e2023GL104391. https://doi.org/10.1029/2023GL104391.

Goldberg, D.E., Yeck, W.L., Hanagan, C.E., Atterholt, J., Kehoe, H., Reitman, N.G., Barnhart, W.D., Shelly, D.R., Hatem, A.E., Wald, D., Earle, P.S., 2025. Ultralong, supershear rupture of the 2025 Mw 7.7 Mandalay earthquake reveals unaccounted risk. Science.

Huang, Z., Zhao, D., Wang, L., 2015. *P* wave tomography and anisotropy beneath Southeast Asia: insight into mantle dynamics: *p* WAVE ANISOTROPY TOMOGRAPHY IN SE ASIA. J. Geophys. Res. Solid. Earth. 120, 5154–5174. https://doi.org/10.1002/2015JB012098.

Hurukawa, N., Maung Maung, P., 2011. Two seismic gaps on the Sagaing fault, Myanmar, derived from relocation of historical earthquakes since 1918: two seismic gaps on the sagaing fault. Geophys. Res. Lett. 38. https://doi.org/10.1029/2010GL046099 n/a-n/a.

Islam, M.M., Wei, S., Persaud, P., Steckler, M.S., Tilmann, F., Ni, J., Gaherty, J., Oo, K.M., Than, O., Htwe, Y.M.M., Sandvol, E., 2024. Mantle deformation in the highly oblique indo-burma subduction system inferred from shear wave splitting measurements. Earth. Planet. Sci. Lett. 643, 118895. https://doi.org/10.1016/j.epsl.2024.118895.

Ji, S., Salisbury, M.H., Hanmer, S., 1993. Petrofabric, P-wave anisotropy and seismic reflectivity of high-grade tectonites. Tectonophysics 222, 195–226. https://doi.org/10.1016/0040-1951(93)90049-P.

Ji, S., Shao, T., Michibayashi, K., Oya, S., Satsukawa, T., Wang, Q., Zhao, W., Salisbury, M.H., 2015. Magnitude and symmetry of seismic anisotropy in mica- and amphibole-bearing metamorphic rocks and implications for tectonic interpretation of seismic data from the southeast Tibetan Plateau. J. Geophys. Res. Solid Earth 120, 6404–6430. https://doi.org/10.1002/2015JB012209.

Kaminski, É., Ribe, N.M., 2002. Timescales for the evolution of seismic anisotropy in mantle flow. Geochem. Geophys. Geosyst. 3, 1–17. https://doi.org/10.1029/2001GC000222.

Khin, K., Zaw, K., Aung, L.T., 2017. Geological and Tectonic Evolution of the Indo-Myanmar Ranges (IMR) in the Myanmar region, 48. Geological Society, London, Memoirs, pp. 65–79. https://doi.org/10.1144/M48.4.

Lee, H.Y., Chung, S.L., Yang, H.M., 2016. Late Cenozoic volcanism in central Myanmar: geochemical characteristics and geodynamic significance. Lithos. 245, 174–190. https://doi.org/10.1016/j.lithos.2015.09.018.

Li, C., van der Hilst, R.D., Meltzer, A.S., Engdahl, E.R., 2008. Subduction of the Indian lithosphere beneath the Tibetan Plateau and Burma. Earth. Planet. Sci. Lett. 274, 157–168. https://doi.org/10.1016/j.epsl.2008.07.016.

Lindsey, E.O., Kuo, Y.T., Wang, Y., Thant, M., Tin, T.Z.H., 2025. Mature fault mechanics revealed by the highly efficient 2025 Mandalay earthquake. Nat. Commun. 16, 10937. https://doi.org/10.1038/s41467-025-65942-2.

Lomax, A., Virieux, J., Volant, P., Berge-Thierry, C., 2000. Probabilistic earthquake location in 3D and layered models. In: Thurber, C.H., Rabinowitz, N. (Eds.), Advances in Seismic Event Location, Modern Approaches in Geophysics. Springer, Netherlands, Dordrecht, pp. 101–134. https://doi.org/10.1007/978-94-015-9536-0_5.

Lü, Y., Ni, S., Chen, L., Chen, Q.-F., 2017. *Pn* tomography with Moho depth correction from eastern Europe to western China: *pn* tomography from Europe to China. J. Geophys. Res. Solid. Earth. 122, 1284–1301. https://doi.org/10.1002/2016JB013052.

Luo, S., Qian, J., 2012. Fast sweeping methods for factored anisotropic eikonal equations: multiplicative and additive factors. J. Sci. Comput. 52, 360–382. https://doi.org/10.1007/s10915-011-9550-y.

Marguin, V., Simpson, G., 2023. Influence of fluids on earthquakes based on numerical modeling. J. Geophys. Res. Solid. Earth. 128, e2022JB025132. https://doi.org/10.1029/2022JB025132.

Maurin, T., Rangin, C., 2009. Structure and kinematics of the Indo-Burmese wedge: recent and fast growth of the outer wedge: growth of the outer indo-burmese wedge. Tectonics 28. https://doi.org/10.1029/2008TC002276 n/a-n/a.

Maury, R.C., Pubellier, M., Rangin, C., Wulput, L., Cotten, J., Socquet, A., Bellon, H., Guillaud, J.-P., Htun, H.M., 2004. Quaternary calc-alkaline and alkaline volcanism in an hyper-oblique convergence setting, central Myanmar and western Yunnan. Bulletin de la Société Géologique de France 175, 461–472. https://doi.org/10.2113/175.5.461.

Metcalfe, I., 2011. Tectonic framework and phanerozoic evolution of Sundaland. Gondwana Res. 19, 3–21. https://doi.org/10.1016/j.gr.2010.02.016.

Mohanty, D.D., Biswal, S., Yoshizawa, K., 2024. Decoupled deformation between crust and mantle beneath Indo-Burmese Wedge: a new seismotectonic model. Earth. Planet. Sci. Lett. 648, 119089. https://doi.org/10.1016/j.epsl.2024.119089.

Mon, C.T., Gong, X., Wen, Y., Jiang, M., Chen, Q., Zhang, M., Hou, G., Thant, M., Sein, K., He, Y., 2020. Insight into major active faults in Central Myanmar and the related geodynamic sources. Geophys. Res. Lett. 47. https://doi.org/10.1029/2019GL086236.

Mon, C.T., Yang, S., Ren, C., He, Y., Thant, M., Sein, K., 2023. New insight into the subducted Indian plate beneath Central Myanmar based on seismic activity and focal mechanisms analysis. Seismol. Res. Lett. https://doi.org/10.1785/0220220381.

Morishita, T., Soe, H.M., Htay, H., Lwin, T.H., Guotana, J.M., Tamura, A., Mizukami, T., Zaw, K., 2023. Origin and evolution of Ultramafic Rocks along the Sagaing Fault. Myanmar J. Earth Sci. 34, 122–132. https://doi.org/10.1007/s12583-021-1435-x.

Münchmeyer, J., 2024. PyOcto: a high-throughput seismic phase associator. Seismica 3. https://doi.org/10.26443/seismica.v3i1.1130.

Plomerová, J., Babuška, V., 2010. Long memory of mantle lithosphere fabric — European LAB constrained from seismic anisotropy. Lithos. Lithosph. Asthenosph. Bound. Nat. Form. Evol. 120, 131–143. https://doi.org/10.1016/j.lithos.2010.01.008.

Savage, M.K., 1999. Seismic anisotropy and mantle deformation: what have we learned from shear wave splitting? Rev. Geophys. 37, 65–106. https://doi.org/10.1029/98RG02075.

Searle, M.P., Morley, C.K., Waters, D.J., Gardiner, N.J., Htun, U.K., Nu, T.T., Robb, L.J., 2017. Tectonic and Metamorphic Evolution of the Mogok Metamorphic and Jade Mines Belts and Ophiolitic Terranes of Burma (Myanmar), 48. Geological Society, London, Memoirs, pp. 261–293. https://doi.org/10.1144/M48.12.

Steckler, M.S., Mondal, D.R., Akhter, S.H., Seeber, L., Feng, L., Gale, J., Hill, E.M., Howe, M., 2016. Locked and loading megathrust linked to active subduction beneath the Indo-Burman ranges. Nat. Geosci. 9, 615–618. https://doi.org/10.1038/ngeo2760.

Takei, Y., 2002. Effect of pore geometry on V/V: from equilibrium geometry to crack. J. Geophys. Res. Solid. Earth. 107. https://doi.org/10.1029/2001JB000522. ECV 6-1-ECV 6-12.

Tin, T.Z.H., Nishimura, T., Hashimoto, M., Lindsey, E.O., Aung, L.T., Min, S.M., Thant, M., 2022. Present-day crustal deformation and slip rate along the southern Sagaing fault in Myanmar by GNSS observation. J. Asian Earth. Sci. 228, 105125. https://doi.org/10.1016/j.jseaes.2022.105125.

Tong, P., 2021. Adjoint-State traveltime tomography for azimuthally anisotropic Media and insight into the crustal structure of Central California near Parkfield. J. Geophys. Res. Solid. Earth. 126, e2021JB022365. https://doi.org/10.1029/2021JB022365.

Tong, P., Yang, D., Huang, X., 2019. Multiple-grid model parametrization for seismic tomography with application to the San Jacinto fault zone. Geophys. J. Int. 218, 200–223. https://doi.org/10.1093/gji/ggz151.

Waldhauser, F., Ellsworth, W.L., 2000. A double-difference earthquake location algorithm: method and application to the Northern Hayward Fault, California. Bull. Seismol. Soc. Am. 90, 1353–1368. https://doi.org/10.1785/0120000006.

Wang, X., Wei, S., Wang, Y., Maung Maung, P., Hubbard, J., Banerjee, P., Huang, B.-S., Moe Oo, K., Bodin, T., Foster, A., Almeida, R., 2019. A 3-D shear wave velocity model for Myanmar region. J. Geophys. Res. Solid. Earth. 124, 504–526. https://doi.org/10.1029/2018JB016622.

Wang, Y., Sieh, K., Tun, S.T., Lai, K., Myint, T., 2014. Active tectonics and earthquake potential of the Myanmar region. J. Geophys. Res. Solid. Earth. 119, 3767–3822. https://doi.org/10.1002/2013JB010762.

Watanabe, T., 1993. Effects of water and melt on seismic velocities and their application to characterization of seismic reflectors. Geophys. Res. Lett. 20, 2933–2936. https://doi.org/10.1029/93GL03170.

Wei, S., Wang, X., Li, C., Zeng, H., Ma, Z., Shi, Q., Chen, H., Huang, Y., Lyu, M., Liao, J., Yang, S., Bai, Y., Maung, P.M., Oo, K., Htwe, Y.M.M., Zhang, J., Dal Zilio, L., Shan, X., Chen, L., 2025. Supershear rupture sustained through a thick fault zone in the 2025 Mw 7.8 Mandalay earthquake. Science 390, 468–475. https://doi.org/10.1126/science.adz2101.

Westerweel, J., Roperch, P., Licht, A., Dupont-Nivet, G., Win, Z., Poblete, F., Ruffet, G., Swe, H.H., Thi, M.K., Aung, D.W., 2019. Burma Terrane part of the Trans-Tethyan arc during collision with India according to palaeomagnetic data. Nat. Geosci. 12, 863–868. https://doi.org/10.1038/s41561-019-0443-2.

Wu, S., Yao, J., Wei, S., Hubbard, J., Wang, Y., Min Htwe, Y.M., Thant, M., Wang, X., Wang, K., Liu, T., Liu, Q., Tong, P., 2021. New insights into the structural heterogeneity and geodynamics of the Indo-Burma subduction zone from ambient noise tomography. Earth. Planet. Sci. Lett. 562, 116856. https://doi.org/10.1016/j.epsl.2021.116856.

Yang, S., Xiao, Z., Wei, S., He, Y., Mon, C.T., Hou, G., Thant, M., Sein, K., Jiang, M., 2024. New insights into active faults revealed by a deep-learning-based earthquake catalog in central Myanmar. Geophys. Res. Lett. 51, e2023GL105159. https://doi.org/10.1029/2023GL105159.

Yao, J., Liu, S., Wei, S., Hubbard, J., Huang, B., Chen, M., Tong, P., 2021. Slab models beneath Central Myanmar revealed by a joint inversion of regional and teleseismic traveltime data. J. Geophys. Res. Solid. Earth. 126. https://doi.org/10.1029/2020JB020164.

Zhang, G., He, Y., Ai, Y., Jiang, M., Mon, C.T., Hou, G., Thant, M., Sein, K., 2021a. Indian continental lithosphere and related volcanism beneath Myanmar: constraints from local earthquake tomography. Earth. Planet. Sci. Lett. 567, 116987. https://doi.org/10.1016/j.epsl.2021.116987.

Zhang, P., Mei, L., Jiang, S.-Y., Xu, S., Donelick, R.A., Li, R., Zhang, H., 2021b. Erosion and sedimentation in SE Tibet and Myanmar during the evolution of the Burmese continental margin from the late cretaceous to early Neogene. Gondwana Res. 95, 149–175. https://doi.org/10.1016/j.gr.2021.04.005.

Zhang, S., Karato, S., 1995. Lattice preferred orientation of olivine aggregates deformed in simple shear. Nature 375, 774–777. https://doi.org/10.1038/375774a0.

Zhao, D., Mishra, O.P., Sanda, R., 2002. Influence of fluids and magma on earthquakes: seismological evidence. Phys. Earth Planet Inter. 132, 249–267. https://doi.org/10.1016/S0031-9201(02)00082-1.

Zhao, D., Yu, S., Liu, X., 2016. Seismic anisotropy tomography: new insight into subduction dynamics. Gondwana. Res. SI Converg. Margins Relat. Process. 33, 24–43. https://doi.org/10.1016/j.gr.2015.05.008.

Zhao, M., Xiao, Z., Chen, S., Fang, L., 2022. DiTing: a large-scale Chinese seismic benchmark dataset for artificial intelligence in seismology. DZXBYWB 36, 84–94. https://doi.org/10.1016/j.eqs.2022.01.022.

Zheng, T., He, Y., Ding, L., Jiang, M., Ai, Y., Mon, C.T., Hou, G., Sein, K., Thant, M., 2020. Direct structural evidence of Indian continental subduction beneath Myanmar. Nat. Commun. 11, 1944. https://doi.org/10.1038/s41467-020-15746-3.

Zhu, W., Beroza, G.C., 2019. PhaseNet: a deep-neural-network-based seismic arrival-time picking method. Geophys. J. Int. 216, 261–273. https://doi.org/10.1093/gji/ggy423.